

Towards high-cooperativity strong coupling of a quantum dot in a tunable microcavity

Lukas Greuter, Sebastian Starosielec, Andreas V. Kuhlmann, and Richard J. Warburton

Department of Physics, University of Basel, Klingelbergstrasse 82, Basel 4056, Switzerland

(Received 22 April 2015; revised manuscript received 5 June 2015; published 9 July 2015)

We investigate the strong-coupling regime of a self-assembled quantum dot in a tunable microcavity with dark-field laser spectroscopy. The high quality of the spectra allows the line shapes to be analyzed revealing subtle quantum interferences. Agreement with a model calculation is achieved only by including exciton dephasing which reduces the cooperativity from a bare value of 9.0 to the time-averaged value 5.5. In the pursuit of high cooperativity, besides a high Q and low mode-volume cavity, we demonstrate that equal efforts need to be taken towards lifetime-limited emitter linewidths.

DOI: [10.1103/PhysRevB.92.045302](https://doi.org/10.1103/PhysRevB.92.045302)

PACS number(s): 42.50.Pq, 42.50.-p, 42.50.Ex, 68.65.Hb

I. INTRODUCTION

Cavity quantum electrodynamics (QED) involves an exchange of energy quanta between a single emitter and a cavity photon. The coupling rate $\hbar g = \mu_{12} E_{\text{vac}}$, depending on the emitter's dipole moment μ_{12} and the vacuum electric field at the location of the emitter E_{vac} , sets the relevant time scale of the coupled dynamics. If g is considerably smaller than the emitter relaxation rate γ or the cavity photon decay rate κ , on resonance the cavity mode acts as an additional decay channel to the emitter giving rise to an enhanced spontaneous emission rate (the Purcell effect of the weak-coupling regime). If g is much larger than the energy loss rates, a coherent exchange of energy quanta takes place giving rise to new eigenstates, “polaritons,” split in energy by $2\hbar g$ (the strong-coupling regime). The efficacy of the coherent coupling is commonly denoted by the cooperativity parameter $C = 2g^2/(\kappa\gamma)$, the figure of merit for this work. The coherent exchange was first realized with single Cs atoms in a high-finesse cavity [1].

The strong-coupling regime is a potentially powerful tool in quantum information processing [2], notably in quantum networks [3], since it enables for instance atom-atom entanglement [4] or the distribution of quantum states [5]. Furthermore, strong coupling enables a nonlinear photon-photon interaction and hence the observation of photon blockade [6,7], a prerequisite for the creation of a single-photon transistor [8,9].

It is clearly desirable to implement cavity QED in the solid state as the solid-state host acts as a natural trap for the emitter. Furthermore, on-chip integration of multiple elements is feasible. As emitter, self-assembled quantum dots have desirable properties: high oscillator strength, narrow linewidths, and weak phonon coupling [10]. As host, a semiconductor such as GaAs is very versatile: heterostructures can be realized; there is a wide array of postgrowth processing techniques. Photoluminescence experiments on single InGaAs SAQD coupled to a photonic crystal cavity or a micropillar cavity revealed an anticrossing, the signature of the strong-coupling regime [11–13]. For micropillars, recent experiments exhibit cooperativity values of around $C \simeq 3$ [14]. For photonic crystal cavities, a much higher C is achieved [15] but C is skewed by the fact that $g \gg \gamma$ yet $g \gtrsim \kappa$. The photon decay rate κ at the emitter wavelength is relatively high in both geometries, limiting the cooperativity. In addition, micropillars and photonic crystals offer only limited spectral tuning to the emitter transition, and spatial positioning of the emitter relative

to the cavity antinode is achieved either by good fortune or by fabricating the cavity around a particular emitter [16,17]. These are challenging issues resulting in a low yield.

In this work we demonstrate a strong coupling of a single self-assembled InGaAs quantum dot to a fully tunable, miniaturized Fabry-Perot cavity [18,19]. The coupled emitter-cavity system is investigated by dark-field laser spectroscopy, yielding extremely high spectral resolution, high sensitivity, a high contrast, and good mode matching. The strong-coupling regime is accessed definitively: we reach a cooperativity of $C = 5.5$, significantly larger than that achieved with micropillars [14] or a fiber cavity [20]. The high quality of the data allows for a quantitative line-shape analysis. We demonstrate an interference in the polariton gap. However, the interference is less pronounced than expected from the “standard model,” the Jaynes-Cummings Hamiltonian. We show that the missing interference arises as a consequence of an additional emitter broadening. Including the emitter broadening allows us to reproduce both the exact line shapes and polariton eigenenergies with a single parameter set for all cavity-emitter detunings. A key point emerges. Achieving a high cooperativity requires more than a focus on the cavity properties (small mode volume and high Q factor): this has to be matched with an equal effort on improving the linewidth of the emitter. Here, we show that suppressing the emitter broadening would yield a cooperativity as high as $C = 9.0$ even with the present microcavity. Characterization of the quantum dots shows that here the main emitter broadening arises from a spectral fluctuation (rather than a true dephasing process): the fluctuations can be circumvented in lower-noise devices. Our system therefore represents an extremely promising route to implementing cavity QED in the solid state.

II. SETUP

The emitter is a self-assembled InGaAs quantum dot grown by MBE at UCSB California. The background doping is small and p type. The details of the heterostructure are depicted in Fig. 1(b): a 32.5 pair $\lambda/4$ AlGaAs/GaAs distributed Bragg reflector (DBR) is terminated by a λ layer of GaAs which incorporates the InGaAs quantum dots in the center. Further details of the sample are given in Appendix A. The bottom DBR with reflectivity $R_{\text{bot}} = 99.99\%$ forms the planar end mirror of the cavity. The concave top mirror consists of a fused silica substrate with a depression formed by CO₂ laser ablation

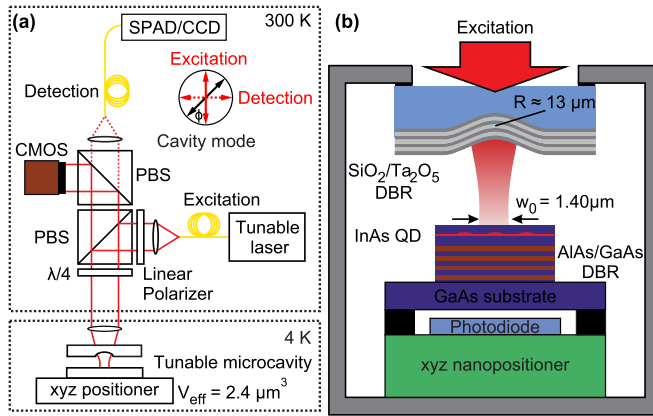


FIG. 1. (Color online) (a) Experimental setup to probe the cavity–quantum dot system. The microscope head is at room temperature and consists of two polarizing beam splitters (PBS), a linear polarizer, and a $\lambda/4$ wave plate. (b) Microcavity setup with a GaAs/AlGaAs bottom mirror and a curved top mirror with radius of $13 \mu\text{m}$ coated with $\text{Ta}_2\text{O}_5/\text{SiO}_2$ DBR. The InGaAs quantum dots are embedded in a semiconductor heterostructure, at distance $\lambda/2$ from the surface and $\lambda/2$ from the bottom mirror.

[21], and is coated with a $\text{Ta}_2\text{O}_5/\text{SiO}_2$ DBR of reflectivity $R_{\text{top}} = 99.95\%$. The radius of curvature is approximately $13 \mu\text{m}$. The bottom semiconductor sample is mounted on an xyz piezo stack that allows for sub-nm positioning with respect to the top mirror enabling both spectral and spatial tuning. The whole microcavity is then mounted on another xyz piezo stack that allows the microcavity to be positioned with respect to an aspherical coupling lens ($\text{NA} = 0.55$), facilitating efficient mode matching with the excitation beam. A Si photodiode mounted underneath the bottom mirror is used for transmission measurements to characterize and optimize the mode matching. By determining the longitudinal mode index $q_0 = 2\partial L/\partial\lambda = 18$, we estimate an effective cavity length of $L = q_0\lambda/2 = 8.5 \mu\text{m}$. From these parameters, a Gaussian optics estimate results in a beam waist of $w_0 = 1.4 \mu\text{m}$ at the sample. The cavity finesse is 4000; the quality factor is $Q = 6 \times 10^4$.

III. EXCITATION AND DETECTION

We measure the coupled cavity–quantum dot dynamics with confocal cross-polarized dark-field laser spectroscopy [22], sketched in Fig. 1(a). The polarizing beam splitters (PBS) define two orthogonal linearly polarized arms (excitation and detection) each coupled to the microcavity via the same objective lens. A linear polarizer and a quarter-wave plate mounted on piezo-driven rotational stages compensate for small imperfections in the optics and enable a suppression of the excitation laser of 10^{-7} to be reached, stable over several days. The cavity exhibits nondegenerate linearly polarized longitudinal modes with a splitting of about $200 \mu\text{eV}$, conveniently larger than the bandwidth required to probe fully the dynamics of the strong coupling. The cavity modes are aligned with respect to the polarization axis of the microscope at an angle $\phi \approx \pi/4$ allowing a good coupling of the cavity mode to both detection and excitation channels. We measure the

wavelength of the tunable excitation laser with a wavemeter and use this information to calibrate the cavity detuning on applying a voltage to the microcavity z piezo. While the polarization optics are all at room temperature, the microcavity setup is inserted into a stainless steel tube containing He exchange gas and cooled to 4 K in a He bath cryostat.

IV. EXPERIMENTAL RESULTS

Tuning the microcavity resonance with respect to the emitter transition, and sweeping the excitation frequency with respect to the microcavity resonance, reveals the exact line shape of the coupled emitter-cavity system for various detunings, as shown in Fig. 2(a). We observe a triplet structure featuring the bare-cavity resonance ω_C along with two detuning-dependent resonances identified as the polariton states of the strong-coupling regime. The bare-cavity contribution can be determined accurately from the data in the polariton gap at zero detuning. A subtraction of the bare-cavity resonance from the raw data reveals the clear anticrossing of the polariton modes, Fig. 2(b).

The anticrossing feature in Fig. 2 is visible only if the sample is illuminated with an additional ultraweak non-resonant excitation laser ($\lambda = 830 \text{ nm}$). In free-space laser spectroscopy experiments on a sample from the same MBE, an “optical gating” by weak nonresonant excitation is described [23]. However, it is only partially successful: observation of the bare-cavity mode shows that the quantum dot detunes abruptly (and out of resonance with the microcavity) in a telegraph fashion. A bare-cavity contribution to resonance spectra has been observed also on photonic crystal cavities [13] and was attributed to charge noise in the vicinity of the quantum dot, a mechanism which is active here. The experiment integrates over a much longer time scale than is typical for this telegraph noise, thus capturing photons from the scattering off the bare cavity a significant fraction of time. We do not observe a

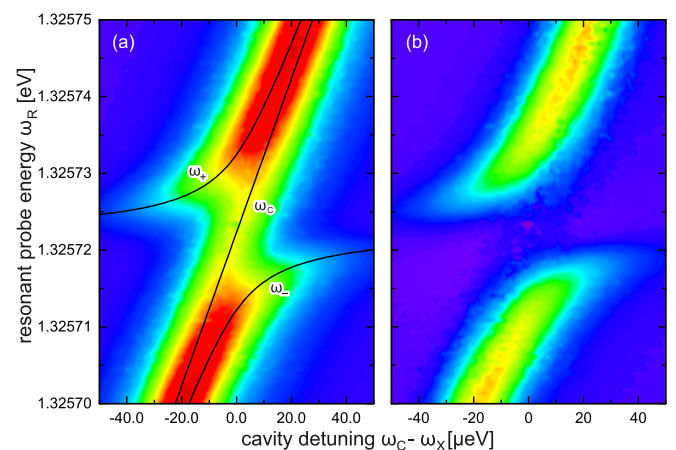


FIG. 2. (Color online) Dark-field resonant laser spectroscopy on a coupled quantum dot–cavity system for varying cavity detuning. (a) A triplet is observed at resonances $\omega_R = \omega_{\pm}, \omega_C$. We interpret the spurious (bare) cavity resonance ω_C as a consequence of an unstable emitter state resulting in telegraph-like dynamics. (b) The data in (a) after subtracting the bare-cavity resonance revealing the normal-mode splitting characteristic of the strong-coupling regime.

fine-structure splitting of the exciton at zero magnetic field. A neutral exciton without fine structure is unlikely for these quantum dots [24] so that we can safely assume that the studied exciton coupling to the cavity in Fig. 2 is a charged exciton.

V. MODEL

We model the experiment with the Jaynes-Cummings Hamiltonian modified for coherent excitation at frequency ω_R :

$$\mathcal{H} = \hbar\omega_C a^\dagger a + \hbar\omega_X b^\dagger b + [\hbar g a^\dagger b + \hbar\epsilon a^\dagger e^{-i\omega_R t} + \text{H.c.}]. \quad (1)$$

Here, a (b) is the bosonic (fermionic) annihilation operator of the microcavity photon (exciton transition) with energy $\hbar\omega_C$ ($\hbar\omega_X$); g denotes the coherent coupling rate between photon and exciton; and ϵ is the effective coupling rate from the resonant excitation to the cavity field. Losses in the system are described by the Lindblad formalism including the photon energy loss rate κ and the exciton relaxation rate γ . The cavity emission is modeled to be weakly coupled to a continuum of detection modes with overall collection efficiency η : the detected count rate is thus $\dot{N} = \eta\kappa\langle a^\dagger a \rangle$.

With model M1 we investigate the system's response as a function of the resonant probe frequency ω_R , treating ϵ as a perturbative parameter. The linear coupling gives rise to two polariton modes (\pm) at Rabi frequencies ω_\pm . The steady-state cavity population (proportional to the photon count rate) evaluates to

$$\langle a^\dagger a \rangle(\omega_R) = A_-^L \mathcal{L}(\omega_R - \omega_-) + A_+^L \mathcal{L}(\omega_R - \omega_+) + A^D \mathcal{D}(\omega_R - \omega_+) - A^D \mathcal{D}(\omega_R - \omega_-), \quad (2)$$

where $\mathcal{L}(\omega) = \text{Im}[(\pi\omega)^{-1}]$ is the unit-area Lorentzian function and $\mathcal{D}(\omega) = \text{Re}[(\pi\omega)^{-1}]$ its dispersive function counterpart, each with peak location $\text{Re}\omega = 0$ and FWHM parameter $2|\text{Im}\omega|$. The peak areas A_\pm^L , A^D and Rabi frequencies ω_\pm are closed form functions of the dynamical parameters ($g, \kappa, \gamma, \epsilon$); see Appendix B.

VI. ANALYSIS

Figure 3 shows (black dots) two exemplary line shapes, (a) for zero cavity-emitter detuning $\omega_C - \omega_X = 0 \mu\text{eV}$, and (b) for significant detuning $\omega_C - \omega_X = -17 \mu\text{eV}$. The purple solid line shows a best χ^2 fit of the observed counts to the model M1, Eq. (2), where the fit results in a single set of dynamical parameters ($g, \kappa, \gamma, \epsilon$), a set used for all employed detunings (Table I). The green and blue solid lines show the Lorentzian and dispersive constituents of the model, while the black dashed line represents the spurious bare-cavity contribution. The dynamical parameters obtained from the fit result in a cooperativity of $C = 2g^2/(\kappa\gamma) = 5.5 \pm 0.1$.

Qualitatively, the model M1 agrees well with the observed polariton resonances in terms of splitting, linewidths as well as their shift with cavity-emitter detuning. Quantitatively, however, the count rates within the polariton gap are significantly underestimated with respect to the experimental data for all detunings. In the polariton gap, the model (neglecting of course the bare-cavity contribution) predicts a strong destructive interference: the positive Lorentzian contributions are reduced considerably by the two dispersive constituents, both of which

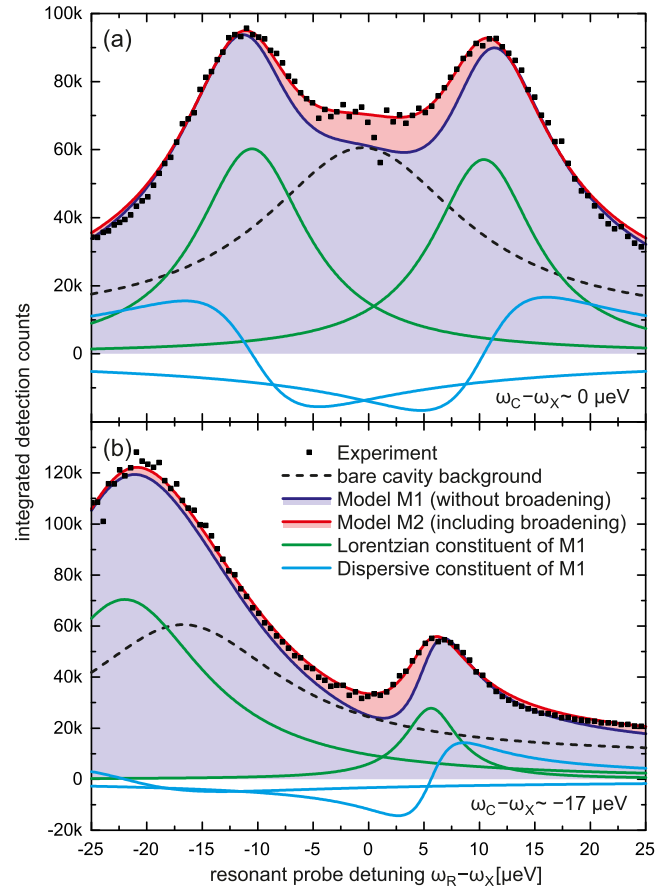


FIG. 3. (Color online) Dark-field laser spectroscopy: spectra for (a) zero and (b) $-17 \mu\text{eV}$ cavity-emitter detuning. The experimental values (black dots) are globally fitted to model M1 (purple solid line), with Lorentzian and dispersive constituents (green and blue solid line), and to model M2 (red solid line). M2, which includes an additional broadening mechanism of the emitter, describes the experimental data much better than M1. The improvement is partially masked by the bare-cavity resonance background (black dashed line).

turn negative. In the experiment, this interference is observed to a lesser degree than that predicted by model M1. This lack of interference is particularly prominent for large detunings

TABLE I. Quantitative fit results of the dynamical parameters for model M1 (no emitter broadening) and for model M2 (with emitter broadening Γ).

Quantity	Unit	Model M1	Model M2
g	$\mu\text{eV}/\hbar$	11.05(2)	11.13(2)
κ	$\mu\text{eV}/\hbar$	19.48(9)	19.84(9)
γ	$\mu\text{eV}/\hbar$	2.28(4)	1.38(4)
Γ	$\mu\text{eV}/\hbar$		1.26(5)
$\eta\kappa t \epsilon ^2$	Mcount $(\mu\text{eV}/\hbar)^2$	6.15(4)	7.08(4)
$C = 2g^2/(\kappa\gamma)$		5.5(1)	9.0(3)
reduced χ^2		123	94

^aWith integration time $t = 20$ s and η the overall collection efficiency of the cavity emission.

TABLE II. Experimental results on the bare-emitter system for QD₁₋₃.

Quantity	Unit	QD ₁	QD ₂	QD ₃
λ	nm	941.79	937.41	939.04
ξ_0	nW	7.0(5)	10.3(9)	20.3(65)
$(\epsilon\xi_2)^{-1}$	μW	0.111(9)	0.55(8)	0.113(51)
Γ_0	μeV	3.84(4)	3.17(8)	3.10(2)
γ_{sw}	μeV	1.4(3)	0.2(3)	1.5(1)
γ_{pd}	μeV	≈ 1.6	^a	≈ 0.8

^aNo consistent determination of γ_{sw} was found for QD₂.

at the exciton-like polariton resonance [Fig. 3(b)] and points strongly to an emitter dynamic not considered by the model.

To investigate this missing dynamic, we performed independent linewidth measurements on the same sample region but without the top mirror. The linewidths are measured under the same conditions, i.e., with resonant laser spectroscopy in the presence of an ultraweak nonresonant excitation (see Appendix E). The results demonstrate a significant contribution to the exciton linewidth beyond that determined by spontaneous emission: typical linewidths are 3–4 μeV ; the radiative-lifetime limited linewidth (the “transform limit”) corresponds to 0.8 μeV . There are two culprits for this additional broadening: a spectral fluctuation (i.e., a wandering of the exciton central frequency on time scales longer than the radiative decay time) and pure exciton dephasing. The analysis (Table II) suggests spectral fluctuations are dominant, but the exact conclusion is quantum-dot dependent. Linewidth broadening on this scale is commonly observed and arises from electric charge noise [25].

As a refinement to the previous model, we incorporate an emitter broadening by convoluting the emitter resonance ω_X with a Lorentzian distribution of free FWHM parameter Γ : this is model M2. The convolution gives an analytical result, Eq. (C6). A fit to the complete experimental data determines the dynamical parameters ($g, \kappa, \gamma, \epsilon, \Gamma$), as shown in Table I. The model M2 results are shown in Fig. 3 as the red solid line. The reduced χ^2 is reduced by 25% but remains high (Table I) but nonetheless M2 offers a strong improvement in the interpretation of the experimental data. This is also demonstrated in Fig. 4: the parameters A_{\pm}^L , A^D , and ω_{\pm} from Eq. (2) are shown from both models M1 and M2 along with the experimental data. M2 significantly improves the FWHM parameters $2\text{Im}\omega_{\pm}$ and Lorentzian areas A_{\pm}^L at all cavity-exciton detuning ranges. Also, M2 resolves the discrepancy in the polariton gap in Fig. 3: M2 accounts perfectly for the experimental data both at zero detuning and at large negative detuning. Only M2 is consistent with the experimental data. The microcavity experiment is therefore sensitive to the emitter linewidth in a way that low-power laser spectroscopy alone is not. (We note that the microcavity experiment cannot distinguish easily between a spectral fluctuation and pure exciton dephasing: the M2 predictions are very similar; see discussion in Appendix C). The increase in emitter linewidth has a major effect on the cooperativity, Table I: M2 shows that emitter broadening alone reduces C from 9.0, the “bare” value, to 5.5.

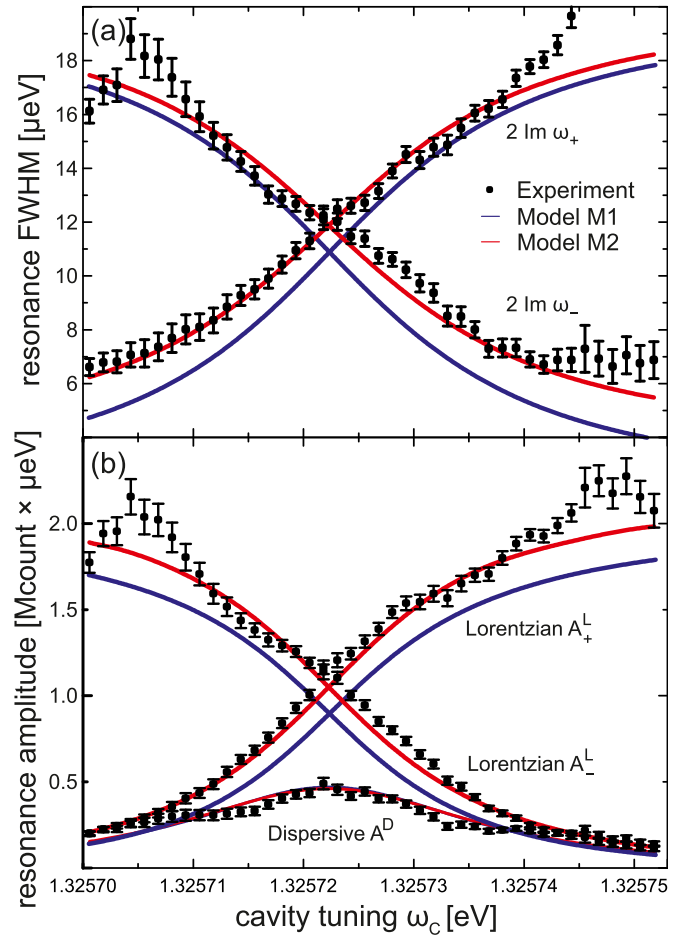


FIG. 4. (Color online) Comparison of models M1 and M2 with the experimental data over the whole cavity-emitter tuning range. (a) The polariton FWHM parameter ($2\text{Im}\omega_{\pm}$) and (b) the Lorentzian/dispersive areas A_{\pm}^L , A^D versus cavity detuning. M2 provides a much better fit than M1.

VII. DISCUSSION

The dynamical parameters of the experiment are summarized in Table I. The free-space emitter lifetime of 800 ps corresponds to a transform-limited linewidth $\gamma = 0.8 \mu\text{eV}$ and a dipole moment $\mu_{12} = 1.2 e \times \text{nm}$. The microcavity Q factor $Q = 6 \times 10^4$ results in $\kappa = 22 \mu\text{eV}$. From a simulation of the microcavity, a vacuum electric field maximum of $E_{\text{vac}} \simeq 2 \times 10^4 \text{ V/m}$ is expected, yielding $g = \mu_{12} E_{\text{vac}} \simeq 24 \mu\text{eV}$. Experimentally, g is smaller than this best-case estimate. From model M1 a cooperativity of $C = 2g^2/(\kappa\gamma) = 5.5 \pm 0.1$, a result depending only weakly on the model assumptions.

An obvious route to higher cooperativity for the presented microcavity system is to improve the mirrors, i.e., to reduce the photon loss rate κ . Presently, the dielectric DBR is the limiting factor and this can be readily improved with “supermirror” coatings [26]. The coupling g should also be improved: presently, slight errors in the microcavity manufacture reduce g from its best-case value. Further, g would increase by a factor of $\sqrt{2}$ (the cooperativity by a factor of 2) if the mode splitting in the fundamental cavity mode (presently $\approx 200 \mu\text{eV}$) could be eliminated. However, the point we wish to stress in this

work is the equal importance of the emitter dynamics. If the additional broadening can be eliminated by improved emitter quality, the cooperativity can be increased from $C = 5.5$ to $C = 9.0$ even without an improvement in the microcavity. This is an entirely realistic proposition: approaches exist by which the additional broadening is routinely sub- μeV [27], in certain cases eliminated altogether [28], without telegraph-like noise by embedding the quantum dots in a vertical tunneling structure. Such a scheme is realistic in the cavity geometry by exploiting the good optical properties of epitaxial gates. The present experiment demonstrates that the use of such emitters will easily allow a cooperativity exceeding 10 to be achieved, a powerful route to the application of cavity QED to quantum control in the solid state.

ACKNOWLEDGMENTS

We thank P. M. Petroff for provision of the semiconductor wafer; we acknowledge financial support from NCCR QSIT and from SNF Project No. 200020_156637.

APPENDIX A: SAMPLE STRUCTURE

A self-assembled InGaAs quantum dot is positioned at the cavity-mode electric-field antinode, as depicted in Fig. 5(a). The heterostructure was grown by molecular beam epitaxy by P. Petroff at UCSB California, and consists of a 100 nm GaAs smoothing layer on a GaAs substrate, and a 32.5 pair

$\lambda/4$ AlGaAs/GaAs distributed Bragg reflector (DBR) as the bottom mirror of the microcavity, which is terminated by a λ -layer GaAs host matrix. During growth, the InGaAs wetting layer is inserted at a $\lambda/2$ distance from the sample surface [Fig. 5(b)]. The top mirror is produced by CO_2 laser ablation from a fused silica substrate, where a concave depression with radius of curvature $\approx 13 \mu\text{m}$ is created before a Ta_2O_5 DBR coating is applied by ion-beam sputtering. The nominal reflectivities are $R_{\text{bot}} = 99.99\%$ and $R_{\text{top}} = 99.95\%$. The bottom mirror is mounted on an xyz piezo-driven positioner for sub-nm positioning, allowing both spectral and spatial tuning of the microcavity. Estimating from Gaussian optics a beam waist of $w = 1.4 \mu\text{m}$ at the quantum dot position from the cavity geometry, with one-dimensional transfer matrix method calculations we estimate a vacuum electric field of $E_{\text{vac}} \approx 2 \times 10^4 \text{ V/m}$. At 4 K, single quantum dots can be addressed in the wavelength range of $930 \dots 960 \text{ nm}$.

APPENDIX B: MODEL CALCULATION (M1)

The model Hamiltonian of the article reads, in the rotating frame of the coherent excitation at frequency ω_R ,

$$\mathcal{H} = \hbar(\omega_C - \omega_R) a^\dagger a + \hbar(\omega_X - \omega_R) b^\dagger b + \hbar g (a^\dagger b + b^\dagger a) + \hbar \epsilon (a^\dagger + a), \quad (\text{B1})$$

where a denotes the bosonic annihilation operator of the cavity (C) and b the fermionic annihilation operator of the exciton transition (X). Here, g is the coherent cavity-exciton coupling rate, and ϵ is the coherent excitation rate driving the bare-cavity resonance from an external laser field whose linewidth is neglected. Treating ϵ as a perturbation parameter, in the absence of other pumping mechanisms the resulting field amplitudes will be of order $a, b \propto \epsilon$.

The coherent and incoherent evolution of the density matrix ρ is given by the Lindblad operator description

$$\begin{aligned} \frac{d\rho}{dt} = & \frac{i}{\hbar} [\rho, \mathcal{H}] + \frac{\kappa}{2} (2a\rho a^\dagger - a^\dagger a \rho - \rho a^\dagger a) \\ & + \frac{\gamma_g}{2} (2b\rho b^\dagger - b^\dagger b \rho - \rho b^\dagger b) \\ & + \frac{\gamma_{\text{pd}}}{4} (b_z \rho b_z - \rho), \end{aligned} \quad (\text{B2})$$

with the cavity photon loss rate κ of the single-cavity mode under consideration; γ_g denotes the exciton's spontaneous emission rate into other guided modes of the cavity. For completion, we also consider an exciton pure dephasing contribution γ_{pd} (where $b_z = 1 - 2b^\dagger b$), whose effect on the dynamics is considered further below.

Observables O inherit a time-dependent expectation value $\langle O \rangle(t) = \text{Tr}[\rho(t)O]$ from the density matrix. The expectation values of the lowest orders of normal-ordered field operators yield a set of optical Bloch equations

$$\frac{d}{dt} \langle a^\dagger \rangle = \left[i(\omega_C - \omega_R) - \frac{\kappa}{2} \right] \langle a^\dagger \rangle + ig \langle b^\dagger \rangle + i\epsilon, \quad (\text{B3a})$$

$$\begin{aligned} \frac{d}{dt} \langle b^\dagger \rangle = & \left[i(\omega_X - \omega_R) - \frac{\gamma_g + \gamma_{\text{pd}}}{2} \right] \langle b^\dagger \rangle + ig \langle a^\dagger \rangle \\ & - 2ig \langle a^\dagger b^\dagger b \rangle, \end{aligned} \quad (\text{B3b})$$

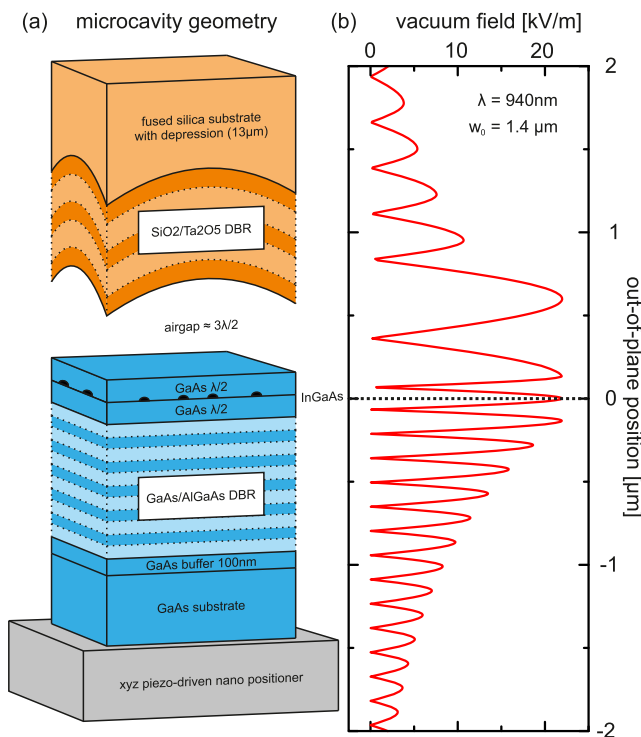


FIG. 5. (Color online) (a) Sample structure within cavity configuration and (b) estimated vacuum field distribution for the design wavelength of $\lambda = 940 \text{ nm}$. The field distribution is estimated from one-dimensional transfer matrix methods, with a Gaussian beam waist of $w_0 = 1.4 \mu\text{m}$.

$$\frac{d}{dt}\langle a^\dagger a \rangle = -\kappa\langle a^\dagger a \rangle - [ig\langle a^\dagger b \rangle + i\epsilon\langle a^\dagger \rangle + \text{H.c.}], \quad (\text{B3c})$$

$$\frac{d}{dt}\langle b^\dagger b \rangle = -\gamma_g\langle b^\dagger b \rangle + [ig\langle a^\dagger b \rangle + \text{H.c.}], \quad (\text{B3d})$$

$$\frac{d}{dt}\langle b^\dagger a \rangle = \left[i(\omega_X - \omega_C) - \frac{\gamma_g + \gamma_{pd} + \kappa}{2} \right] \langle b^\dagger a \rangle + ig(\langle a^\dagger a \rangle - \langle b^\dagger b \rangle) - i\epsilon\langle b^\dagger \rangle - 2ig\langle a^\dagger b^\dagger ab \rangle. \quad (\text{B3e})$$

The higher-order terms $\langle a^\dagger b^\dagger b \rangle$ and $\langle a^\dagger b^\dagger ab \rangle$ originate from the fermionic nature of the exciton after applying the commutator rule $[b, b^\dagger] = 1 - 2b^\dagger b$ and thus represent all saturation effects. At weak excitations $\epsilon \propto b \ll 1$ these contributions are suppressed and are further neglected. For vanishing pure dephasing rate $\gamma_{pd} \ll \gamma_g$, the set of optical Bloch equations are solved by the ansatz $\langle a^\dagger a \rangle = \langle a^\dagger \rangle \langle a \rangle$, $\langle b^\dagger b \rangle = \langle b^\dagger \rangle \langle b \rangle$, and $\langle b^\dagger a \rangle = \langle b^\dagger \rangle \langle a \rangle$ with $\langle a^\dagger \rangle$ and $\langle b^\dagger \rangle$ the solution to Eqs. (B3a) and (B3b). The steady state ($d/dt \equiv 0$) yields

$$\langle a^\dagger \rangle = \frac{\epsilon(\omega_X - \omega_R + i\frac{\gamma_g}{2})}{g^2 - (\omega_X - \omega_R + i\frac{\gamma_g}{2})(\omega_C - \omega_R + i\frac{\kappa}{2})} \quad (\text{B4a})$$

$$= \frac{\epsilon_+^a}{\omega_R - \omega_+} + \frac{\epsilon_-^a}{\omega_R - \omega_-}, \quad (\text{B4b})$$

$$\langle b^\dagger \rangle = \frac{\epsilon g}{g^2 - (\omega_X - \omega_R + i\frac{\gamma_g}{2})(\omega_C - \omega_R + i\frac{\kappa}{2})} \quad (\text{B4c})$$

$$= \frac{\epsilon_+^b}{\omega_R - \omega_+} + \frac{\epsilon_-^b}{\omega_R - \omega_-}. \quad (\text{B4d})$$

As a function of the resonant probe ω_R , a double pole structure arises at complex Rabi frequencies

$$\omega_\pm = \frac{\omega_C + \omega_X}{2} + i\frac{\kappa + \gamma_g}{4} \pm \sqrt{g^2 + \left(\frac{\omega_C - \omega_X}{2} + i\frac{\kappa - \gamma_g}{4} \right)^2} \quad (\text{B5})$$

with projected excitation rates

$$\epsilon_\pm^a = \frac{\epsilon}{2} \left[1 \pm \frac{\frac{\omega_C - \omega_X}{2} + i\frac{\kappa - \gamma_g}{4}}{\sqrt{g^2 + \left(\frac{\omega_C - \omega_X}{2} + i\frac{\kappa - \gamma_g}{4} \right)^2}} \right], \quad (\text{B6a})$$

$$\epsilon_\pm^b = \mp \frac{\epsilon}{2} \left[\frac{g}{\sqrt{g^2 + \left(\frac{\omega_C - \omega_X}{2} + i\frac{\kappa - \gamma_g}{4} \right)^2}} \right]. \quad (\text{B6b})$$

So far, the detection channel has not been explicitly modeled. A weak coupling of the cavity to a continuum of lossy detection modes contributes a photon flux of $\eta\kappa\langle a^\dagger a \rangle$ to the observed intensity, where the collection efficiency η has no dependence on the cavity tuning. In the weak-excitation regime, both the absolute value of $\langle a^\dagger a \rangle$ and the excitation rate ϵ are difficult to determine experimentally. We note that the detected intensity is proportional to $\langle a^\dagger a \rangle$, and limit our study to its dependence on ω_R . A partial fraction decomposition of

the absolute square of $\langle a^\dagger \rangle$ from Eq. (B4a) yields

$$\begin{aligned} \langle a^\dagger a \rangle &= [V_+ + \text{Re } W]\mathcal{L}(\omega_R - \omega_+) + \text{Im } W\mathcal{D}(\omega_R - \omega_+) \\ &\quad + [V_- + \text{Re } W]\mathcal{L}(\omega_R - \omega_-) - \text{Im } W\mathcal{D}(\omega_R - \omega_-), \end{aligned} \quad (\text{B7})$$

i.e., a sum of unit-area Lorentzian and corresponding dispersive function line shapes,

$$\mathcal{L}(\omega_R - \omega_\pm) = \frac{\text{Im } \omega_\pm / \pi}{(\omega_R - \text{Re } \omega_\pm)^2 + (\text{Im } \omega_\pm)^2}, \quad (\text{B8a})$$

$$\mathcal{D}(\omega_R - \omega_\pm) = \frac{(\omega_R - \text{Re } \omega_\pm) / \pi}{(\omega_R - \text{Re } \omega_\pm)^2 + (\text{Im } \omega_\pm)^2}, \quad (\text{B8b})$$

with magnitudes

$$V_\pm = \frac{\pi |\epsilon_\pm^a|^2}{\text{Im } \omega_\pm} \quad \text{and} \quad W = 2\pi i \frac{\epsilon_+^a \epsilon_-^{a*}}{\omega_+ - \omega_-^*}, \quad (\text{B9})$$

where (*) denotes complex conjugation. The line-shape resonances are located at $\text{Re } \omega_\pm$ with FWHM parameter $2|\text{Im } \omega_\pm|$. The result for $\langle b^\dagger b \rangle$ is analogous to Eq. (B7), with ϵ^b substituted into the magnitudes Eq. (B9).

APPENDIX C: MODEL CALCULATION (M2)

Model M1 assumes that the exciton behaves as a perfect two-level system. In model M2 we introduce two major broadening mechanisms of the exciton and calculate their effects on the resonance line shapes. One mechanism is a pure dephasing, i.e., an additional loss of exciton coherence in addition to radiative decay; the second mechanism is a spectral wandering, i.e., a temporal fluctuation of the bare-exciton transition frequency ω_X . The dynamics under pure dephasing are governed by the Lindblad operator contribution proportional to γ_{pd} , the last term in Eq. (B2). We implement the spectral wandering by a convolution of the observable $\langle a^\dagger a \rangle$ with a distribution of ω_X with FWHM parameter γ_{sw} . As long as γ_{sw} is much smaller than the observed linewidths $\approx \kappa$, the details of the distribution shape are insignificant. For the sake of analytical simplicity, we choose a Lorentzian distribution.

The optical Bloch equations (B3) can be solved analytically for a nonzero pure dephasing rate γ_{pd} within the weak-excitation regime. The ω_R dependence of the result is

$$\langle a^\dagger a \rangle = \langle a^\dagger a \rangle' + \frac{C_{pd}}{|\omega_R - \omega_+|^2 |\omega_R - \omega_-|^2}, \quad (\text{C1})$$

where the primed expressions correspond to the previous results when γ_g is renormalized by $\gamma_g \rightarrow \gamma_g + \gamma_{pd}$. The correction amplitude C_{pd} is given by

$$\begin{aligned} C_{pd} &= 4|\epsilon|^2 g^4 \frac{\gamma_{pd} \kappa + \gamma_g + \gamma_{pd}}{\gamma_g \kappa} \left[4g^2 \frac{(\kappa + \gamma_g)(\kappa + \gamma_g + \gamma_{dp})}{\kappa \gamma_g} \right. \\ &\quad \left. + (\kappa + \gamma_g + \gamma_{dp})^2 + 4(\omega_C - \omega_X)^2 \right]^{-1}. \end{aligned} \quad (\text{C2})$$

In the experimental regime of the article ($g \approx 10 \mu\text{eV}$, $\kappa \approx 20 \mu\text{eV}$, $\gamma_g \approx 2 \mu\text{eV}$) we expect only a weak dependence of C_{pd} on the experimental control parameters, namely the cavity detuning $\omega_C - \omega_X$.

The Lorentzian convolution (*) of $\langle a^\dagger a \rangle$, Eq. (B7), with respect to ω_X with FWHM parameter γ_{sw} is based on the algebraic form of Eq. (B4a). Observing the identity

$$\left| \frac{\omega_X - A}{\omega_X - B} \right|^2 * \mathcal{L}_{sw} = \left| \frac{\omega_X - A'}{\omega_X - B'} \right|^2 - \frac{\pi \gamma_{sw}}{4} \frac{|A - B|^2}{\text{Im } B \text{ Im } B'} \mathcal{L}_{B'}(\omega_X) \quad (\text{C3})$$

valid in the regime $\text{Im } A, \text{Im } B < 0$, we identify $A = \omega_R - i\gamma_g/2$ and $B = A + g^2/(\omega_C - \omega_R + i\kappa/2)$. The primed expressions are renormalized according to $\gamma_g \rightarrow \gamma_g + \gamma_{sw}$. Here, $\mathcal{L}_{B'}$ is a Lorentzian located at $\text{Re } B'$ with FWHM parameter $2 \text{Im } B'$. Similar to the pure-dephasing case, we find a corresponding algebraic structure

$$\langle a^\dagger a \rangle = \langle a^\dagger a \rangle' + \frac{C_{sw}}{|\omega_R - \omega'_+|^2 |\omega_R - \omega'_-|^2} \quad (\text{C4})$$

with the correction amplitude from spectral wandering

$$C_{sw} = 4|\epsilon|^2 g^4 \frac{\gamma_{sw}}{\gamma_g} \left[4g^2 \frac{\kappa}{\gamma_g} + \kappa^2 + 4(\omega_R - \omega_C)^2 \right]^{-1}. \quad (\text{C5})$$

Different from the pure dephasing case, the correction amplitude for spectral wandering C_{sw} depends on $\omega_R - \omega_C$. However, as for C_{pd} , the dependence on experimental parameters (ω_R, ω_C) is only weak as $g \approx \kappa \gg \gamma_g$.

Treating both correction amplitudes C_{pd}, C_{sw} as approximately constant, the emitter broadening induces, along with the renormalization of γ_g , a correction to the Lorentzian and dispersive line-shape constituents according to

$$\langle a^\dagger a \rangle = \langle a^\dagger a \rangle' + \text{Re } U_+ \mathcal{L}(\omega_R - \omega'_+) + \text{Im } U_+ \mathcal{D}(\omega_R - \omega'_+) + \text{Re } U_- \mathcal{L}(\omega_R - \omega'_-) + \text{Im } U_- \mathcal{D}(\omega_R - \omega'_-), \quad (\text{C6})$$

with amplitudes

$$U_\pm = \frac{\pi}{\text{Im } \omega'_\pm} \frac{C}{(\omega'_\pm - \omega'_\mp)(\omega'_\pm - \omega'^{*}_\mp)}. \quad (\text{C7})$$

From symmetry we find $\text{Im } U_+ = -\text{Im } U_-$. In the strong-coupling regime, and also for large cavity-emitter detuning, U_\pm is largely real valued. Hence we expect as the main signature of emitter broadening a significant increase of the Lorentzian line-shape contribution, while the dispersive line-shape constituent remains unaffected.

APPENDIX D: CONTRIBUTION TO SIGNAL FROM EXCITON DECAY

We address the role of the bare-exciton population $\langle b^\dagger b \rangle$ whose contribution to the detection signal is expected to be negligible as the experiment is performed in a confocal detection scheme such that the coupling to the bare-cavity mode only is efficient. From the model M1 Eq. (B4) we find

$$\frac{\langle b^\dagger b \rangle}{\langle a^\dagger a \rangle} = \frac{g^2}{(\omega_X - \omega_R)^2 + (\gamma_g/2)^2}; \quad (\text{D1})$$

i.e., a parasitic contribution from $\langle b^\dagger b \rangle$ to the detection signal must show the following signatures: (i) be proportional to $\langle a^\dagger a \rangle$ and (ii) be strongly enhanced at $\omega_R \approx \omega_X$. Signature (i) is clearly not observed in the experiment: $\langle a^\dagger a \rangle$ is small

in the polariton gap yet the deviation between M1 and the experimental data is largest here. Signature (ii) is not observed for strong cavity-exciton detuning where model M1 perfectly reproduces both cavity-like and exciton-like resonance amplitudes at $\omega_R = \omega_C$ and $\omega_R = \omega_C$, respectively. We thus conclude that the contribution of $\langle b^\dagger b \rangle$ cannot explain the most dominant deviations between model M1 and the experimental results.

APPENDIX E: BARE-EMITTER OPTICAL PROPERTIES

The analysis in Appendix C was limited to the weak-excitation regime where a broadening effect on the emitter can be quantified, while the underlying mechanism (pure dephasing or spectral wandering) remained ambiguous. This limitation is lifted in the strong-excitation regime: when saturation effects become important a distinction can be made. The full cavity-coupled emitter dynamics are difficult to solve; however the bare-emitter dynamics are readily accessible. The bare-exciton emission under resonant excitation—commonly referred to as resonance fluorescence—follows the Hamiltonian

$$\mathcal{H} = \hbar(\omega_X - \omega_R) b^\dagger b + \frac{\hbar\Omega}{2} (b^\dagger + b), \quad (\text{E1})$$

where Ω is the Rabi frequency of the resonant excitation of the emitter. As before, we introduce the radiative decay rate γ in free space and pure dephasing rate γ_{pd} by Lindblad operators. The optical Bloch equations on the exciton population and coherence then read

$$\frac{d}{dt} \langle b^\dagger b \rangle = -\gamma \langle b^\dagger b \rangle - \frac{i\Omega}{2} \langle b^\dagger \rangle + \frac{i\Omega}{2} \langle b \rangle, \quad (\text{E2a})$$

$$\frac{d}{dt} \langle b^\dagger \rangle = \left[i(\omega_X - \omega_R) - \frac{\gamma + \gamma_{dp}}{2} \right] \langle b^\dagger \rangle + \frac{i\Omega}{2} - i\Omega \langle b^\dagger b \rangle. \quad (\text{E2b})$$

The steady-state population results in a Lorentzian line

$$\langle b^\dagger b \rangle = \frac{\Omega^2 \bar{\gamma} / \gamma}{4(\omega_R - \omega_X)^2 + \bar{\gamma}^2 + 2\Omega^2 \bar{\gamma} / \gamma}, \quad (\text{E3})$$

with the combined rate $\bar{\gamma} = \gamma + \gamma_{pd}$. The observed experimental linewidth Γ , when the emitter is subject to an additional broadening due to spectral wandering γ_{sw} , is after Lorentzian convolution

$$\Gamma = \sqrt{\bar{\gamma}^2 + 2\Omega^2 \bar{\gamma} / \gamma} + \gamma_{sw}. \quad (\text{E4})$$

The resonance fluorescence peak intensity $I = \beta \langle b^\dagger b \rangle$ at resonance $\omega_R = \omega_X$ is given by

$$I = \beta \frac{\Omega^2}{\bar{\gamma} \gamma + 2\Omega^2} \times \frac{\Gamma - \gamma_{sw}}{\Gamma} \quad (\text{E5a})$$

$$= I_{\text{sat}} \left(1 - \left[\frac{\Gamma_0 - \gamma_{sw}}{\Gamma - \gamma_{sw}} \right]^2 \right), \quad (\text{E5b})$$

where I_{sat} is the peak intensity at saturation for $\Omega \gg \gamma$, $\Gamma_0 = \gamma + \gamma_{pd} + \gamma_{sw}$ is the linewidth for $\Omega \rightarrow 0$, and β is the overall instrumentation factor. Equation (E5b) expresses the power-dependent resonance fluorescence intensity I in terms

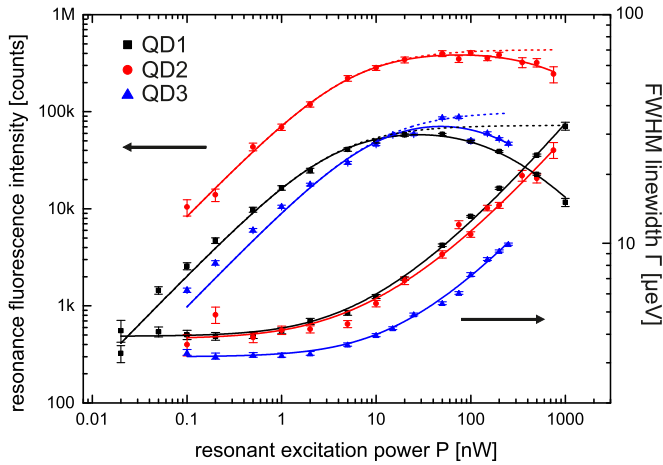


FIG. 6. (Color online) Resonance fluorescence peak intensity (left scale) and FWHM linewidth (right scale) for three investigated quantum dots (symbols). The peak intensity dependence with resonant pump power matches a three-level description to a high degree, where the assumed third level is nonresonantly pumped. From the three-level description we extrapolate to the corresponding two-level dynamics (dashed lines) where the third level is eliminated from the dynamics. The linewidth dependence with resonant pump power is already well reproduced by the two-level description.

of convenient observables I_{sat} and Γ , where β and the Rabi frequency Ω have been eliminated. In the case $\gamma_{\text{sw}} = 0$, the intensity I yields a linear relation to Γ^{-2} with intersects at I_{sat} and T_2 -limited rate $\bar{\gamma}$. A nonvanishing spectral wandering rate $\gamma_{\text{sw}} \neq 0$ violates the linear relation, allowing γ_{sw} to be used as a robust fitting parameter.

We investigate the spectral wandering of single quantum dots in the same sample area and wavelength as in the microcavity experiment of the article. Although the very same quantum dot cannot be conserved between configurations, we assume a close statistical resemblance.

Figure 6 shows as symbols the peak resonance fluorescence intensity I as a function of the resonant excitation power P for three different quantum dots as well as their corresponding resonance FWHM linewidths. In addition to the resonant excitation, we require an ultraweak nonresonant excitation to observe the resonance fluorescence, as was the case in the experiment in the article. Beyond saturation at about 10 nW of monitored resonant excitation power, the resonance fluorescence peak intensity drops with further increase in excitation power, in contrast to the two-level model. We attribute this breakdown to a spurious coupling to a third level (e.g., a different charge state, either the quantum dot or the environment). Indeed from a simple rate equation model, where a third state is nonresonantly driven from either the upper or lower level at smaller rate ϵP , the steady-state population of the upper level is

$$I_3 = \beta \frac{(1 + \epsilon \eta_1)P}{\xi_0 + (2 + \epsilon \xi_1)P + \epsilon \xi_2 P^2}, \quad (\text{E6})$$

where the coefficients $\eta_1 < 1$ and ξ_i depend on the details of the relaxation rates. The power dependence of I_3 in Eq. (E6) is quantitatively well reproduced in the experimental data. Under the assumption $\epsilon \eta_1, \epsilon \xi_1 \ll 1$ we determine ξ_0

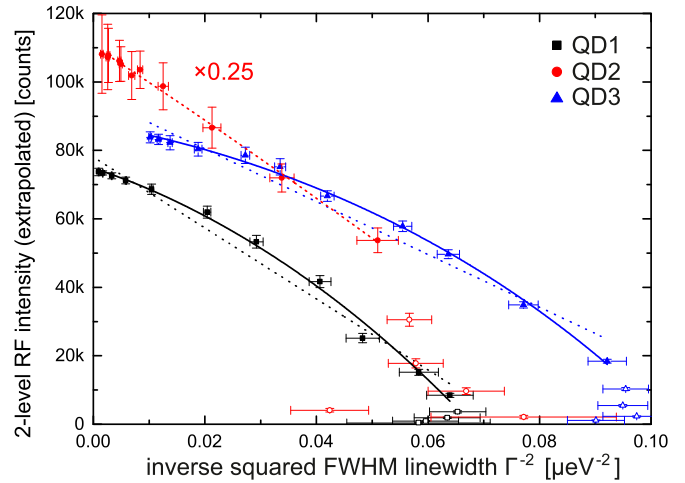


FIG. 7. (Color online) Measurement of the resonance fluorescence peak intensity versus the inverse squared linewidth (symbols) for the three investigated quantum dots. A vanishing spectral wandering rate yields a linear relation (dotted line), while the experimental data are consistent with a spectral wandering rate of $\approx 1.5 \mu\text{eV}$ for QD₁ and QD₃. On QD₂ no consistent determination of the spectral wandering rate is found. The open symbols at very low resonant excitation power have been disregarded from the fit, as the collected intensity is dominated by photoluminescence from an ultraweak nonresonant excitation scheme.

and $(\epsilon \xi_2)^{-1}$ (see Table II). Taking the limit $\epsilon \xi_2 \rightarrow 0$, this allows us to extrapolate from the resonance fluorescence intensity I_3 of the three-level system the expected resonance fluorescence intensity $I_2 = P/(\xi_0 + 2P)$ of an effective two-level system where the third-level contribution is eliminated. The extrapolated intensity is shown in Fig. 6 as a dashed line. In terms of resonance linewidth, the experimental data show no significant deviation from a two-level description.

Figure 7 shows as symbols the resonance fluorescence intensity as a function of the inverse squared linewidth Γ^{-2} for the three investigated quantum dots (filled symbols). At very low resonant excitation powers, the collected intensity is dominated by the photoluminescence intensity from the additional ultraweak nonresonant excitation scheme. For this reason, we discard the data for very low collected intensities (open symbols). Applying the relation Eq. (E5b) to the data, for QD₁ and QD₃, the relation is well reproduced for $\gamma_{\text{sw}} = 1.5 \pm 0.1 \mu\text{eV}$ and $1.4 \pm 0.2 \mu\text{eV}$, respectively (solid line). For comparison the best fit for $\gamma_{\text{sw}} = 0$ (dotted line) is in clear contradiction to the experimental data. For QD₂ no significant spectral wandering is observed; however we note that the relative error on the resonance fluorescence intensity is considerably larger than for the other QDs and no consistent behavior at low intensity is found. Thus on QD₂ no reliable estimation of the spectral wandering rate can be obtained. The T_2 -limited linewidth $\bar{\gamma} = \gamma + \gamma_{\text{pd}} = \Gamma_0 - \gamma_{\text{sw}}$ evaluates to $\approx 2.44 \mu\text{eV}$ ($1.6 \mu\text{eV}$) for QD₁ (QD₃). As the transform-limited radiative decay rate $\gamma \approx 0.8 \mu\text{eV}$, we estimate a corresponding pure dephasing rate of $\gamma_{\text{pd}} \approx 1.6 \mu\text{eV}$ ($\approx 0.8 \mu\text{eV}$) for QD₁ (QD₃).

In summary, we observe that spectral wandering is likely to represent a dominating broadening mechanism in the

investigated sample. This result underlines the major statement of the article: the cavity-coupled exciton cooperativity can

be readily enhanced if the additional emitter broadening, identified as spectral wandering, can be reduced.

-
- [1] A. Boca, R. Miller, K. M. Birnbaum, A. D. Boozer, J. McKeever, and H. J. Kimble, *Phys. Rev. Lett.* **93**, 233603 (2004).
- [2] A. Imamoğlu, D. D. Awschalom, G. Burkard, D. P. DiVincenzo, D. Loss, M. Sherwin, and A. Small, *Phys. Rev. Lett.* **83**, 4204 (1999).
- [3] H. J. Kimble, *Nature (London)* **453**, 1023 (2008).
- [4] M. B. Plenio, S. F. Huelga, A. Beige, and P. L. Knight, *Phys. Rev. A* **59**, 2468 (1999).
- [5] T. Wilk, S. C. Webster, A. Kuhn, and G. Rempe, *Science* **317**, 488 (2007).
- [6] K. M. Birnbaum, A. Boca, R. Miller, A. D. Boozer, T. E. Northup, and H. J. Kimble, *Nature (London)* **436**, 87 (2005).
- [7] A. Reinhard, T. Volz, M. Winger, A. Badolato, K. J. Hennessy, E. L. Hu, and A. Imamoğlu, *Nat. Photonics* **6**, 93 (2012).
- [8] D. E. Chang, A. S. Sørensen, E. A. Demler, and M. D. Lukin, *Nat. Phys.* **3**, 807 (2007).
- [9] T. Volz, A. Reinhard, M. Winger, A. Badolato, K. J. Hennessy, E. L. Hu, and A. Imamoğlu, *Nat. Photonics* **6**, 605 (2012).
- [10] R. J. Warburton, *Nat. Mater.* **12**, 483 (2013).
- [11] J. P. Reithmaier, G. Sek, A. Löffler, C. Hofmann, S. Kuhn, S. Reitzenstein, L. V. Keldysh, V. D. Kulakovskii, T. L. Reinecke, and A. Forchel, *Nature (London)* **432**, 197 (2004).
- [12] T. Yoshie, A. Scherer, J. Hendrickson, G. Khitrova, H. M. Gibbs, G. Rupper, C. Ell, O. B. Shchekin, and D. G. Deppe, *Nature (London)* **432**, 200 (2004).
- [13] K. Hennessy, A. Badolato, M. Winger, D. Gerace, M. Atatüre, S. Gulde, S. Fält, E. L. Hu, and A. Imamoğlu, *Nature (London)* **445**, 896 (2007).
- [14] M. Lerner, N. Gregersen, F. Dunzer, S. Reitzenstein, S. Höfling, J. Mørk, L. Worschech, M. Kamp, and A. Forchel, *Phys. Rev. Lett.* **108**, 057402 (2012).
- [15] D. Englund, A. Faraon, I. Fushman, N. Stoltz, P. Petroff, and J. Vučković, *Nature (London)* **450**, 857 (2007).
- [16] A. Badolato, K. Hennessy, M. Atatüre, J. Dreiser, E. Hu, P. M. Petroff, and A. Imamoğlu, *Science* **308**, 1158 (2005).
- [17] A. Dousse, L. Lanco, J. Suffczyński, E. Semenova, A. Miard, A. Lemaître, I. Sagnes, C. Roblin, J. Bloch, and P. Senellart, *Phys. Rev. Lett.* **101**, 267404 (2008).
- [18] R. J. Barbour, P. A. Dalgarno, A. Curran, K. M. Nowak, H. J. Baker, D. R. Hall, N. G. Stoltz, P. M. Petroff, and R. J. Warburton, *J. Appl. Phys.* **110**, 053107 (2011).
- [19] L. Greuter, S. Starosielec, D. Najer, A. Ludwig, L. Duempelmann, D. Rohner, and R. J. Warburton, *Appl. Phys. Lett.* **105**, 121105 (2014).
- [20] J. Miguel-Sánchez, A. Reinhard, E. Togan, T. Volz, A. Imamoğlu, B. Besga, J. Reichel, and J. Estève, *New J. Phys.* **15**, 045002 (2013).
- [21] D. Hunger, C. Deutsch, R. J. Barbour, R. J. Warburton, and J. Reichel, *AIP Adv.* **2**, 012119 (2012).
- [22] A. V. Kuhlmann, J. Houel, D. Brunner, A. Ludwig, D. Reuter, A. D. Wieck, and R. J. Warburton, *Rev. Sci. Instrum.* **84**, 073905 (2013).
- [23] H. S. Nguyen, G. Sallen, C. Voisin, P. Roussignol, C. Diederichs, and G. Cassaboïs, *Phys. Rev. Lett.* **108**, 057401 (2012).
- [24] S. Seidl, B. D. Gerardot, P. A. Dalgarno, K. Kowalik, A. W. Holleitner, P. M. Petroff, K. Karrai, and R. J. Warburton, *Physica E* **40**, 2153 (2008).
- [25] J. Houel, A. V. Kuhlmann, L. Greuter, F. Xue, M. Poggio, B. D. Gerardot, P. A. Dalgarno, A. Badolato, P. M. Petroff, A. Ludwig, D. Reuter, A. D. Wieck, and R. J. Warburton, *Phys. Rev. Lett.* **108**, 107401 (2012).
- [26] G. Rempe, R. J. Thompson, H. J. Kimble, and R. Lalezari, *Opt. Lett.* **17**, 363 (1992).
- [27] A. V. Kuhlmann, J. Houel, A. Ludwig, L. Greuter, D. Reuter, A. D. Wieck, M. Poggio, and R. J. Warburton, *Nat. Phys.* **9**, 570 (2013).
- [28] A. V. Kuhlmann, J. H. Prechtel, J. Houel, A. Ludwig, D. Reuter, A. D. Wieck, and R. J. Warburton, *arXiv:1307.7109*.